Catalysis Science & Technology

ROYAL SOCIETY OF CHEMISTRY

PAPER

View Article Online
View Journal

Cite this: DOI: 10.1039/d6cy00140h

A facile silicon doping strategy constructing "M–O–Si" bonds in ZnCo-LDH for efficient neutral nitrate reduction to ammonia and Zn–NO_3^- battery

Kunxuan Zhao,†[a] Pei Chen,†[a] Yulan Shi,[a] Zhen Yang,[a] Xia Zhou,[a] Jinfeng Yang,*[a] Xiaodong Yang *[b] and Feng Yu *[a]

The development of efficient electrocatalysts for the nitrate reduction reaction (NO_3^-RR) to ammonia in neutral media is often hindered by complex synthesis methods and insufficient catalytic performance. In this study, we report a highly facile and rapid (30 seconds) room-temperature etching method for synthesizing silicon-doped ZnCo layered double hydroxides (Si-ZnCo-LDH/Cu), which facilitates the formation of abundant "M–O–Si" (M = Zn, Co) linkages. This silicon-induced modulation of the electronic structure significantly enhances NO_3^-RR activity. The Si-ZnCo-LDH/Cu catalyst achieves an ammonia production rate of 25.71 mg h^{-1} cm^{-2} in neutral electrolyte with a Faradaic efficiency of 93.6%, markedly surpassing that of the pristine ZnCo-LDH/Cu (16.03 mg h^{-1} cm^{-2}, 58.4%). Comprehensive experimental and theoretical investigations demonstrate that the "M–O–Si" bond acts as a key active site, promoting electron transfer and optimizing the adsorption of critical intermediates, thereby reducing the energy barrier of the rate-determining step (*NO → *NOH) from 0.97 eV to 0.51 eV and effectively suppressing the competing hydrogen evolution reaction. Furthermore, a Zn–nitrate battery assembled with Si-ZnCo-LDH/Cu delivers a maximum power density of 17 mW cm^{-2}, maintaining stable operation for 60 hours. This work presents a universal and effective doping strategy for the rational design of high-performance layered electrocatalysts.

Received 3rd February 2026,
Accepted 9th February 2026

DOI: 10.1039/d6cy00140h

rsc.li/catalysis

Introduction

Ammonia (NH_3) serves as a vital foundation for global agriculture and the hydrogen economy, yet its production still predominantly relies on the energy-intensive Haber–Bosch process, which operates under extreme temperatures and pressures (500 °C, >200 atm). This process consumes approximately 1–2% of the world's energy annually and is responsible for nearly 160 million metric tons of CO_2.[1–6] On the other hand, growing nitrate contamination in water bodies-primarily originating from industrial and domestic wastewater, fossil fuel combustion, and excessive fertilizer use-poses serious threats to ecosystems and human health.[7–12] Electrochemical nitrate reduction (NO_3^-RR) to NH_3 represents a sustainable and eco-friendly technology, offering a dual benefit of water purification and potential replacement for the carbon-intensive Haber–Bosch process, holding considerable promise for future applications.[13,14] However, the practical implementation of this technology hinges on the development of efficient electrocatalysts capable of driving the complex multi-electron/proton reduction process selectively and actively. It is therefore imperative to design and synthesize such catalysts to unlock the full potential of NO_3^-RR.[15,16]

Layered double hydroxides (LDHs), known for their good electrical conductivity and abundant porosity,[17] effectively facilitate electron transfer and molecular diffusion, making them widely applicable in electrocatalysis. However, the limited variety of active sites in LDHs often hampers the multi-electron/proton transfer processes, thereby suppressing their NO_3^-RR activity. To address this issue, researchers have adopted strategies such as constructing heterostructures and introducing elemental dopants to optimize the chemical and electronic structures of LDHs.[18] For instance, Zhang *et al.* developed a heterostructured electrode composed of NiCo-LDH shell-coated copper nanowires (NiCo-LDH@CuNW), which achieved a Faradaic efficiency for NH_3 of 94.25% and an NH_3 production rate of 46.24 mg h^{-1} cm^{-2} in alkaline electrolyte.[19] Gu *et al.* successfully constructed a heterojunction catalyst integrating Ni_6 clusters with CuFe-LDH nanosheets. Mechanistic studies revealed that the

[a] *Key Laboratory of Silicon Chemical New Materials, School of Chemistry and Chemical Engineering, Shihezi University, Shihezi 832003, P.R. China. E-mail: yufeng05@mail.ipc.ac.cn*
[b] *College of Sciences, Shihezi University, Shihezi 832003, China*
† These authors contributed equally to this work.

synergistic interaction at the heterointerface alters the rate-determining step from NH_3 desorption to the reduction of NO_3^- to NO_2^-, significantly enhancing the nitrate reduction Faradaic efficiency from ~73% for pure CuFe-LDH to ~97%.[20] More recently, Fu *et al.* realized atomically dispersed Cu doping in NiFe-LDH, leading to an NH_3 faradaic efficiency of 90.1% and an NH_3 yield of 3.58 mg h^{-1} cm^{-2}, tripling the performance of the undoped sample.[21] Although current LDH-based catalysts demonstrate promising NO_3^-RR performance for ammonia production, their practical application is constrained by the corrosive nature of alkaline electrolytes (*e.g.*, KOH), which causes device degradation. Therefore, the development of LDH-based electrocatalysts that operate efficiently in neutral electrolytes for NO_3^-RR to ammonia is both essential and imperative.

In this work, we constructed a silicon-doped ZnCo layered double hydroxide (Si-ZnCo-LDH) rich in "M–O–Si" (M = Zn, Co) motifs *via* a $SiCl_4$ liquid-phase etching strategy. The electrode composed of Si-ZnCo-LDH and copper hydroxide delivers outstanding electrocatalytic nitrate reduction performance in a neutral electrolyte (0.5 M Na_2SO_4 + 0.1 M KNO_3) at −1.3 V (*vs.* RHE), achieving an NH_3 production rate of 25.71 mg h^{-1} cm^{-2} and a Faradaic efficiency of 93.61%, substantially surpassing the undoped ZnCo-LDH (16.03 mg h^{-1} cm^{-2}, 58.41%). Moreover, the electrode exhibits an ammonia selectivity of 91.79% and a nitrate removal rate of 97.89%. *In situ* ATR-FTIR, *in situ* Raman spectroscopy, and *in situ* electrochemical mass spectrometry were employed to monitor key intermediates during the NO_3^-RR process, complemented by DFT calculations to assess their adsorption energies. The results indicate that the "M–O–Si" bonds in Si-ZnCo-LDH modulate the electronic structure of the active centers, optimizing the adsorption of *NO and *NOH intermediates and reducing the reaction free energy (ΔG) by 0.46 eV, thereby significantly lowering the energy barrier of the rate-determining step. A Zn–nitrate battery assembled with Si-ZnCo-LDH/Cu demonstrates an open-circuit voltage of 1.43 V and a maximum power density of 17 mW cm^{-2}, along with stable operation over 60 hours at a current density of 10 mA cm^{-2}. The pioneering application of silicon-doped LDH in neutral nitrate reduction offers a novel design strategy for NO_3^-RR electrocatalysts, thereby advancing the development of multi-functional systems for synergistic pollutant conversion, green ammonia production, and power output.

Results and discussion

Catalyst preparation and characterization

As shown in Fig. 1a, ZnCo-LDH nanosheets were first grown *in situ* on chemically etched copper foam *via* electrodeposition, and then reacted with silicon tetrachloride ($SiCl_4$) to obtain Si-ZnCo-LDH. Scanning electron microscopy (SEM) images indicated that $Cu(OH)_2$ showcased a vertically aligned nanorod morphology (Fig. 1b), ZnCo-LDH showed a nanosheet morphology (Fig. 1c). After Si doping, ZnCo-LDH

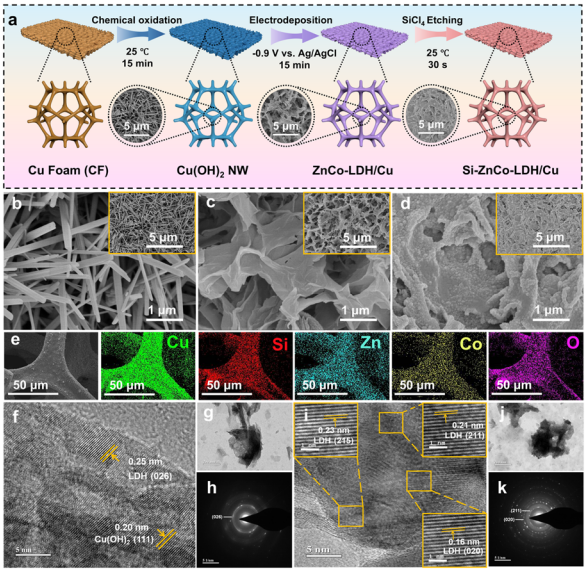

Fig. 1 Catalyst preparation and morphology analysis. (a) Schematic illustration of the fabrication process of Si-ZnCo-LDH/Cu. SEM images (including insets) of (b) $Cu(OH)_2$/CF, (c) ZnCo-LDH/Cu, (d) Si-ZnCo-LDH/Cu. (e) The element mapping images of the Si-ZnCo-LDH/Cu and HRTEM images of (f–h) ZnCo-LDH/Cu, (i–k) Si-ZnCo-LDH/Cu.

nanosheets were cut and curled up, presenting nanoparticle-modified nanosheets (Fig. 1d and S1). Elemental mapping images showed the uniform distribution of Si, Zn, Co, Cu, and O (Fig. 1e). Transmission electron microscopy (TEM) images further confirm the nanosheets morphology of ZnCo-LDH and Si-ZnCo-LDH (Fig. 1g and j). High resolution TEM (HRTEM) images of ZnCo-LDH and Si-ZnCo-LDH both showed clear lattice fringes, confirming their excellent crystallinity (Fig. 1f and i). The interplanar spacing of ZnCo-LDH calculated by the Bragg's Law ($2d \sin\theta = n\lambda$) is 0.25 nm, corresponding to (026) face of LDH. Notably, the 0.21 nm interplanar spacing of Si-ZnCo-LDH (Fig. 1i) assigned to the (211) crystal plane, corresponding to the diffraction peak of 44.1° in XRD pattern.

The X-ray diffraction (XRD) patterns of ZnCo-LDH/Cu and Si-ZnCo-LDH/Cu correspond well with the standard cards of the reported ZnCo-LDH phase[22] (JCPDS#21-1447; Fig. 2a). Moreover, ZnCo-LDH exhibits increased crystallinity after silicon doping. Fourier transform infrared (FT-IR) spectra revealed the formation of "M–O–Si" bonds (Fig. 2b). Si-ZnCo-LDH/Cu showcases an enhanced and broadened absorption peak at 1049 cm^{-1} compared with ZnCo-LDH/Cu, attributing to the asymmetric stretching vibration of the "M–O–Si" (M = Zn, Co) bond. Raman spectroscopy of Si-ZnCo-LDH/Cu demonstrates two new peaks at 292 and 441 cm^{-1} that were assigned to "Si–O–Si" and "M–O–Si" bonds, respectively, further indicating the local structural reconstruction induced by Si doping (Fig. 2c).

X-ray photoelectron spectroscopy (XPS) survey spectrum of Si-ZnCo-LDH/Cu showcase Zn, Co, Cu, O, and Si elements (Fig. 2d). In the Zn 2p spectra (Fig. 2e), ZnCo-LDH/Cu show two characteristic peaks at 1021.67 and

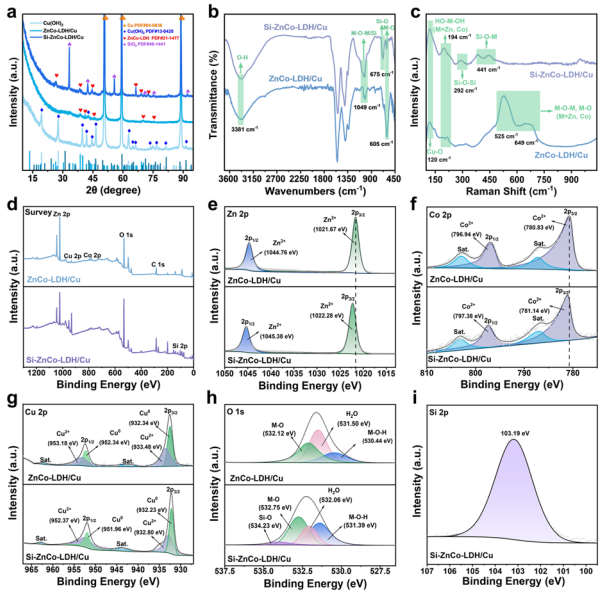

Fig. 2 The chemical state valence state analysis of the catalyst. (a) The XRD patterns, (b) Fourier transform infrared spectroscopy (FTIR), (c) Raman spectroscopy of Si-ZnCo-LDH/Cu and ZnCo-LDH/Cu. (d) The XPS survey, (e) Zn 2p, (f) Co 2p, (g) Cu 2p and (h) O 1s core levels spectrum of Si-ZnCo-LDH/Cu and ZnCo-LDH/Cu. (i) The high-resolution XPS spectra of Si 2p core levels of Si-ZnCo-LDH/Cu.

1044.76 eV, corresponded to $2p_{3/2}$ and $2p_{1/2}$ of Zn^{2+}, respectively. In the Co 2p spectra (Fig. 2f), ZnCo-LDH/Cu showed two characteristic peaks at 780.83 eV and 796.94 eV, respectively, corresponded to $2p_{3/2}$ and $2p_{1/2}$ of Co^{2+}, respectively. Notably, compared with ZnCo-LDH/Cu, all peaks within Zn 2p and Co 2p of Si-ZnCo-LDH/Cu moved towards the higher binding energy, indicating that the silicon doping reduced the electron density of Zn^{2+} and Co^{2+}. In the Cu 2p spectra (Fig. 2g), The peak intensity corresponding to Cu^0 at 932.34 eV increased significantly, whereas the main peaks and satellite features associated with Cu^{2+} at 933.48 eV were attenuated.[23] These changes confirm the Si-induced partial reduction of Cu^{2+} to metallic CuO. In the O 1s spectra (Fig. 2h), three distinct peaks were identified at 532.12 eV, 531.50 eV, and 530.44 eV, attributed to M–O, adsorbed H_2O, and "M–O–M" bonds, respectively.[24] An additional peak observed at 534.23 eV in the Si-doped sample is assigned to Si-O, confirming the formation of "M–O–Si" (M = Zn, Co) interfacial bonds.

Furthermore, the Si 2p spectrum (Fig. 2i) exhibited a characteristic peak at 103.5 eV, ascribed to the "M–O–Si" bond, indicating that Si is incorporated into the LDH structure in the form of silicate. The notable deviation in binding energy from that of elemental silicon (99.3 eV) underscores the formation of strong interfacial bonding.[25] These XPS findings are consistent with the FT-IR results, which also revealed "M–O–Si" and "Si–O–Si" vibrations, collectively providing robust evidence for successful Si doping in the catalyst structure.

Electrochemical performance for NO_3^-RR

The NO_3^-RR performance was evaluated by using a three electrode H-type cell under ambient conditions using 0.5 M Na_2SO_4 as the electrolyte (Fig. S2). Linear sweep voltammetry (LSV) curves of the catalysts were recorded. Noticeably higher current density was observed in the presence of NO_3^- as compared to the counterpart under NO_3^- free conditions (Fig. 3a). We further compared the LSV curves of both catalysts in the absence of NO_3^- (Fig. S3), Si-ZnCo-LDH/Cu exhibits consistently lower current densities than ZnCo-LDH/Cu across all measured potentials (*e.g.*, decreasing from −166 mA cm^{-2} to −126 mA cm^{-2} at −1.3 V *vs.* RHE). This suggested that silicon incorporation intrinsically suppresses the HER activity of the ZnCo-LDH. The product selectivity of Si-ZnCo-LDH/Cu was then assessed by chronoamperometry at a constant potential for 1 h. Ultraviolet-visible (UV-vis) spectrophotometry and calibration curves were employed to quantify the concentrations of NH_3, NO_2^-, and NO_3^- (Fig. S4–S6). Si-ZnCo-LDH/Cu with different dopping time display notable variations in their FE values andNH_3 yields at −1.3 V *vs.* RHE (Fig. 3b and Table S1). In more detail, it was found that Si-ZnCo-LDH/Cu shows a remarkable FE of 93.6% and a NH_3 yield of 25.71 mg h^{-1} cm^{-2}, which is higher than many catalysts under similar conditions (Fig. 3g).[26–37] Both Si-ZnCo-LDH/Cu-15 s and Si-ZnCo-LDH/Cu-45 s present the enhanced FE values and NH_3 yields than that of ZnCo-LDH/Cu. By comparison, Si-ZnCo-LDH/Cu-60 s presents a comparatively low FE of 52.66%, even lower than that of the undoped ZnCo-LDH/Cu. Based on these results, we speculate that the duration of Si doping may affect the structure of the catalyst, which in turn influences the NO_3^-RR performance. Therefore, Si-ZnCo-LDH/Cu was the focus of our study, followed by further testing of the electrochemical NO_3^-RR performance of this catalyst.

Both ZnCo-LDH/Cu and Si-ZnCo-LDH/Cu were assessed at different potentials for 1 h (Fig. S7 and S8 and Table S2). As shown in Fig. 3c, both samples present a nitrate conversion rate exceeding 90% in the voltage range of −1.1 V to −1.5 V *vs.* RHE, which suggest that their comparable ability to reduce NO_3^-. ZnCo-LDH/Cu presents a comparatively low FE of 16.22% and NH_3 yield of 56.37 mg h^{-1} cm^{-2} at −1.1 V *vs.* RHE, and the maximum FE is 64.25% at the cathodic potential of −1.4 V *vs.* RHE (Fig. 3d). Nevertheless, Si-ZnCo-LDH/Cu shows the highest FE of 93.6% and a NH_3 yield of 25.71 mg h^{-1} cm^{-2} at −1.3 V *vs.* RHE (Fig. 3e). The slight decrease in FE and NH_3 yield at more negative potentials can be attributed to the dominance of competitive HER. These results suggest that Si doping not only ensures the efficient conversion of NO_3^- but also improves the selectivity for NH_3 (Fig. S9). Moreover, Si-ZnCo-LDH/Cu can completely degrade all NO_3^- in the electrolyte in just 3 hours. (Fig. 3f). The concentration of the main product NH_4^+-N was as high as 1.3 mg mL^{-1}, and the concentration of the by-product NO_2^--N was only 0.025 mg mL^{-1}, which was significantly better than the catalytic ability of ZnCo-LDH/Cu (Fig. S10).

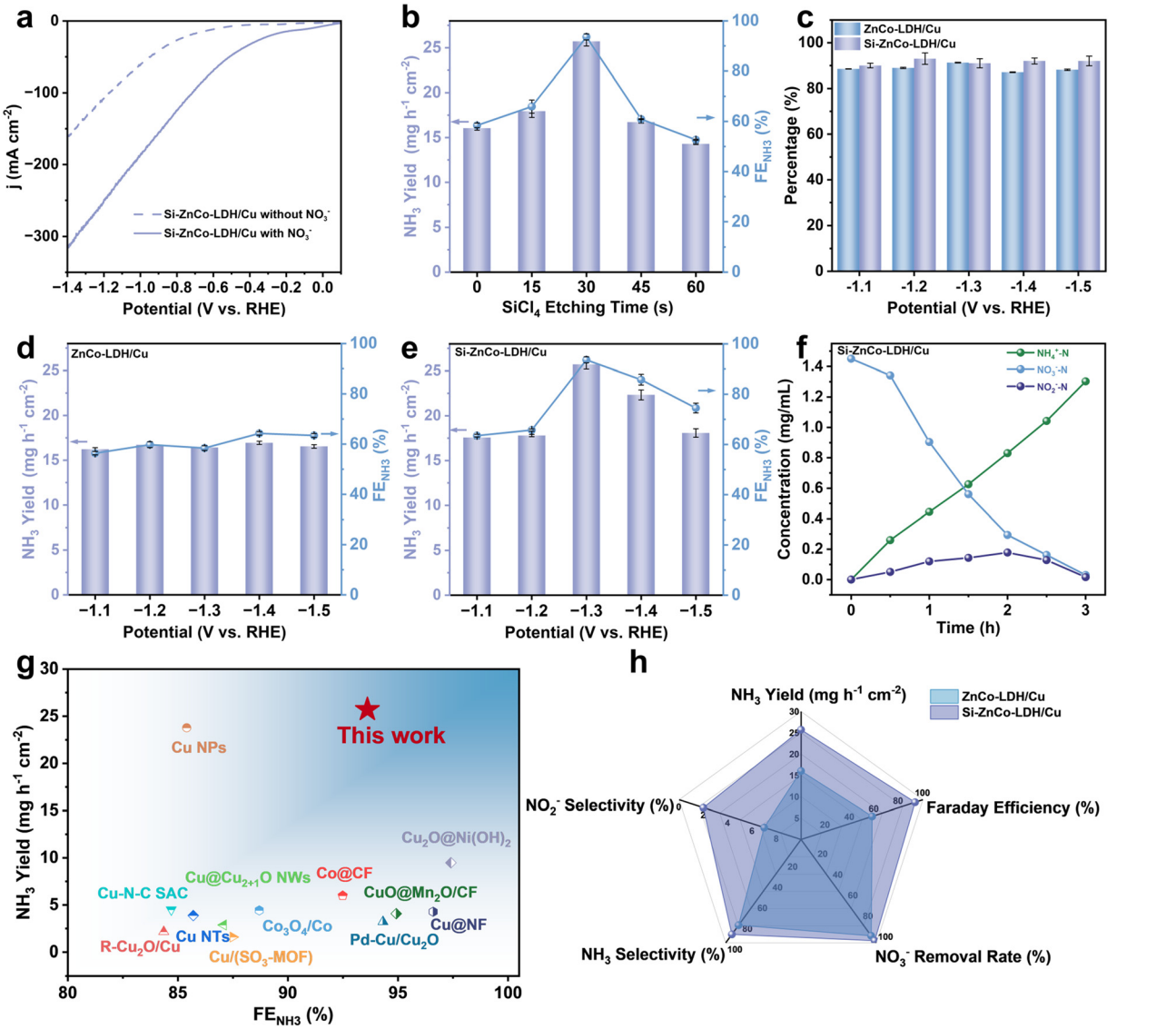

Fig. 3 Electrocatalytic NO_3^-RR performance. (a) LSV of Si-ZnCo-LDH/Cu in 0.5 M Na_2SO_4 electrolyte when NO_3^- is absent (dotted line) and NO_3^- is present (solid line). (b) Ammonia yield and FE_{NH_3} of NO_3^-RR to ammonia over ZnCo-LDH/Cu, Si-ZnCo-LDH/Cu-15 s, Si-ZnCo-LDH/Cu-30 s, Si-ZnCo-LDH/Cu-45 s Si-ZnCo-LDH/Cu-60 s at −1.3 V *vs.* RHE. (c) The nitrate conversion rates of ZnCo-LDH/Cu and Si-ZnCo-LDH/Cu at different potentials. (d) Ammonia yield and FE_{NH_3} of ZnCo-LDH/Cu at different applied potentials. (e) Ammonia yield and FE_{NH_3} of Si-ZnCo-LDH/Cu at different applied potentials. Si-ZnCo-LDH/Cu of (f) the concentrations of NH_4^+-N, NO_3^--N and NO_2^--N in the electrolyte varied with time at −1.3 V *vs.* RHE. (g) The comparison chart of the performance of electrocatalytic NO_3^-RR with other newly reported catalysts. (h) A radar chart showing ammonia yield, FE_{NH_3}, nitrate removal efficiency ammonia selectivity and nitrite selectivity.

The Tafel slopes of different samples indicated that Si doping enhances the electrocatalytic kinetics of ZnCo-LDH/Cu (Fig. S11). Electrochemical impedance spectroscopy (EIS) further revealed that Si doping improves charge transfer efficiency, with Si-ZnCo-LDH/Cu exhibiting the lowest charge transfer resistance (1.36 Ω) among all samples (Fig. S12). We further investigated the influence of Na_2SO_4 electrolyte concentration (0.1 M, 0.5 M, and 1.0 M) on the NO_3^-RR performance of Si-ZnCo-LDH/Cu (Fig. S13), Si-ZnCo-LDH/Cu exhibited slightly inferior NH_3 yield and FE in 0.1 M and 1.0 M Na_2SO_4. We speculated a balance was achieved between charge transport and efficient mass transfer in a 0.5 M Na_2SO_4 electrolyte. To evaluate practical performance under varying conditions, we investigated the influence of initial NO_3^- concentration on the NO_3^-RR performance of Si-ZnCo-LDH/Cu (Fig. S14). Furthermore, after introducing 0.1 M KNO_3, the open-circuit potential (OCP) of Si-ZnCo-LDH/Cu shifted to 0.102 V, significantly higher than the 0.034 V of ZnCo-LDH/Cu (Fig. S15). This indicates a stronger adsorption affinity for NO_3^- after Si doping, which promotes reactant enrichment at active sites and facilitates subsequent electron-transfer steps, thereby improving overall reaction kinetics. To identify the nitrogen source in NH_3 synthesis, controlled experiments confirmed that significant NH_3 production occurred only

with the Si-ZnCo-LDH/Cu catalyst in nitrate- containing solution, whereas yields were negligible with pure Cu foam or in nitrate-free electrolyte (Fig. S16), establishing nitrate as the essential nitrogen precursor. We further investigated the pH adaptability on the NO_3^-RR performance of Si-ZnCo-LDH/Cu (Fig. S17). The catalyst exhibited the highest NH_3 yield and FE under near-neutral pH, while performance declined markedly in acidic or alkaline conditions. This indicates that the "M–O–Si" bond structure stabilizes the catalytic interface effectively under direct application in neutral aqueous environments without requiring extreme pH adjustment. Furthermore, the Si-ZnCo-LDH/Cu electrode demonstrated remarkable stability, maintaining high NH_3 yield and Faradaic efficiency over 10 h of continuous operation at −1.3 V *vs.* RHE (Fig. S18). Furthermore, Si-ZnCo-LDH/Cu also remained robust performance in simulated groundwater containing common interfering ions (*e.g.*, Cl^-, HCO_3^-, Ca^{2+}, Mg^{2+}), with no significant decline after tolerance testing (Fig. S19), underscoring the strong anti-interference ability and structural integrity of the "M–O–Si" active site. Together with an NH_3 selectivity of 91.78%, a nitrate removal rate of 97.89%, a nitrite selectivity of 1.99%, an NH_3 yield of 25.71 mg h^{-1} cm^{-2}, and an NH_3 faradaic efficiency of 93.61% (Fig. 3h), these results affirm the catalyst's high efficiency

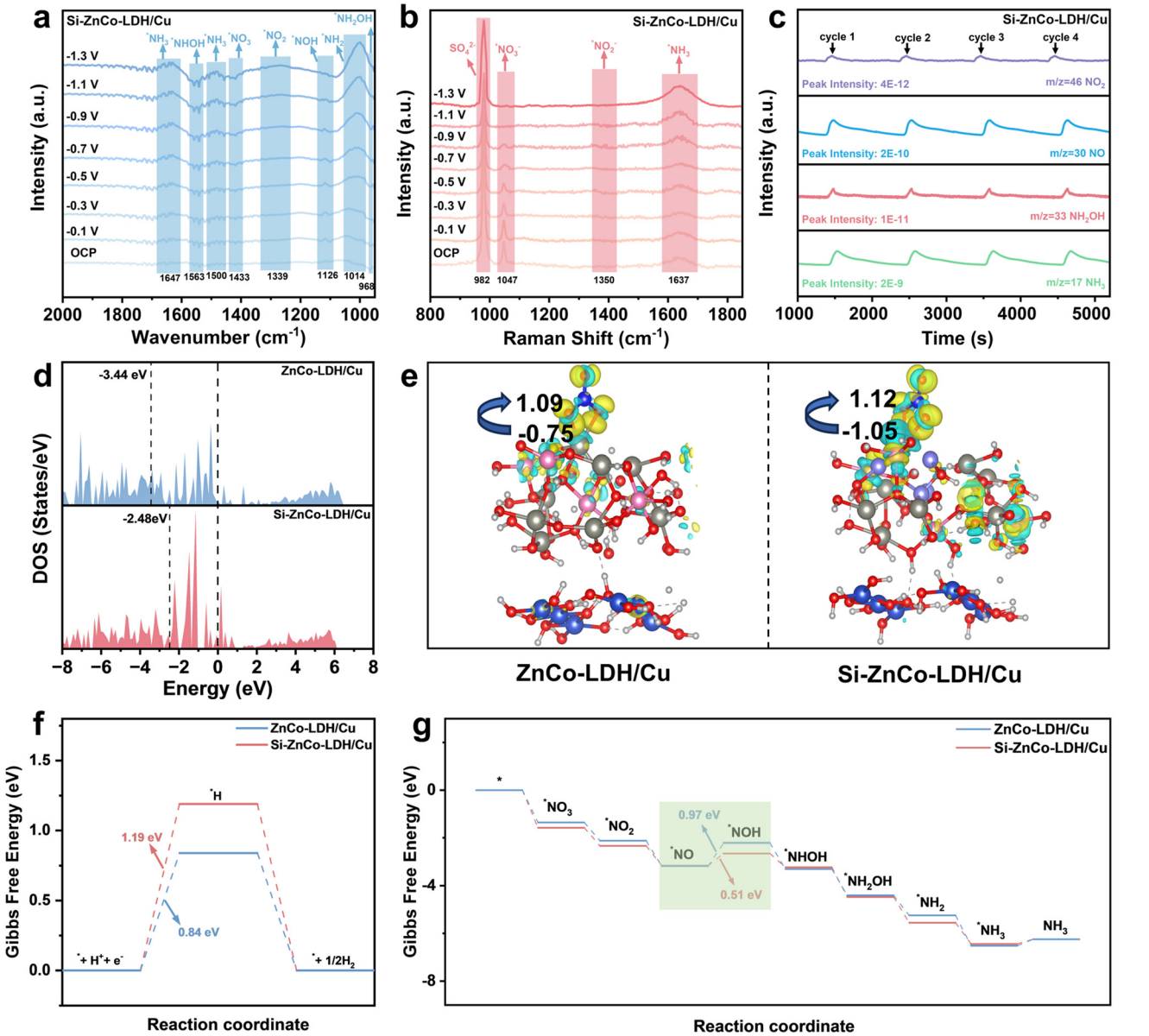

Fig. 4 Mechanism exploration and density functional theory calculation. Si-ZnCo-LDH/Cu (a) electrochemical *in situ* ATR-FTIR spectra. (b) Electrochemical *in situ* Raman spectra. (c) Electrochemical DEMS measurements of NO_3^-RR. (d) The density of states of ZnCo-LDH/Cu and Si-ZnCo-LDH/Cu. (e) Differential charge density of $*NO_3$ of ZnCo-LDH/Cu and Si-ZnCo-LDH/Cu. The isosurface value is set to be 0.02 e $Å^{-3}$, and the consumption and accumulation of charges are shown in yellow and cyan, respectively. Gibbs free energy diagram of (f) HER and (g) various intermediates during the electrocatalytic NO_3^-RR.

and practical potential for selective nitrate-to-ammonia conversion.

Mechanism study

To gain molecular-level insight into the reaction mechanism, we performed *in situ* attenuated total reflection Fourier transform infrared (ATR-FTIR) spectroscopy, *in situ* Raman spectroscopy, and on-line differential electrochemical mass spectrometry (DEMS) to monitor species and intermediates adsorbed on the electrode surface during the NO_3^-RR. The *in situ* ATR-FTIR spectra of the Si-ZnCo-LDH/Cu (Fig. 4a) exhibit eight characteristic absorption bands between OCP and −1.3 V *vs.* RHE. The band at 968 cm^{-1} is assigned to the N–O stretching vibration of $*NH_2OH$. Its intensity first increases and then decreases, suggesting $*NH_2OH$ formation at lower potentials and subsequent reduction to $*NH_2$ at higher potentials. The band at 1014 cm^{-1} corresponds to the N–H bending vibration of $*NH_2$.[38] Its pronounced accumulation implies a more efficient reduction pathway after Si doping, effectively promoting the ammonia synthesis reaction. The band at 1126 cm^{-1} is attributed to the N–O stretching mode of *NOH, a short-lived intermediate that rapidly transforms further. The band at 1339 cm^{-1} represents the symmetric stretching vibration of $*NO_2$,[39] which forms at low potentials and is gradually reduced to *NO as the potential decreases. The band at 1433 cm^{-1} is associated with the asymmetric stretching vibration of $*NO_3$, whose intensity decreases with more negative potential, reflecting the conversion of NO_3^- to other intermediates. The band at 1500 cm^{-1} arises from the N–H bending vibration of $*NH_3$, confirming $*NH_3$ generation.[40] The band at 1563 cm^{-1} reflects the conversion of *NHOH intermediates to ammonia with increasing overpotential. Finally, the band at 1647 cm^{-1} represents the symmetric deformation vibration of $*NH_3$, further indicating increased ammonia production.[41] The *in situ* ATR-FTIR spectra of ZnCo-LDH/Cu (Fig. S20) are largely similar to those of the Si-doped sample, indicating a similar reaction pathway during NO_3^-RR.

In situ Raman spectroscopy was performed over a potential range of OCP to −1.3 V (*vs.* RHE), revealing characteristic vibrational modes associated with nitrate reduction intermediates. As shown in (Fig. 4b), the band centered at 982 cm^{-1} is assigned to the vibrational mode of SO_4^{2-} in the electrolyte solution.[42] The intensity of the latter decreases progressively as the potential shifts negatively and eventually disappears at −1.3 V, indicating efficient and complete reduction of NO_3^-. The peak at 1350 cm^{-1} is attributed to the asymmetric stretching vibration of NO_2^-.[43] It is absent at low potentials, appears as a small broad band at intermediate potentials, and vanishes again at higher potentials, suggesting that NO_2^- is transiently generated and rapidly consumed. The peak at 1637 cm^{-1} represents the symmetric deformation vibration of NH_3,[44] whose intensity increases steadily with more negative potential, reflecting the continuous formation of the main product. Some intermediates (*e.g.*, *NO and *NOH) were not detected due to their low concentration or weak Raman activity, while transient species (*e.g.*, *NHOH and $*NH_2OH$) were difficult to capture owing to their short lifetimes. Silicon doping promotes the dominant reaction pathway ($NO_3^- \rightarrow NO_2^- \rightarrow NH_3$) and suppresses the formation of byproducts (*e.g.*, *NO, *NOH), which explains the absence of their signals. The *in situ* Raman spectra collected on ZnCo-LDH/Cu (Fig. S21) are generally similar to those of the Si-doped sample.

To gain operando insight into the gaseous and volatile intermediates, online differential electrochemical mass spectrometry (DEMS) was employed to monitor the NO_3^-RR process. As the applied potential was swept from OCP to −1.5 V (*vs.* RHE), distinct signals[45] corresponding to NO_2 (m/z = 46), NO (m/z = 30), NH_2OH (m/z = 33), and NH_3 (m/z = 17) were consistently detected over multiple consecutive cycles (Fig. 4c and S22). Integrating these findings with the results from *in situ* ATR-FTIR and *in situ* Raman spectroscopy, we propose a reaction pathway for the electrocatalytic nitrate reduction: NO_3^- is sequentially reduced to NO_2^- and NO, followed by hydrogenation to NH_2OH, and finally to NH_3. This proposed pathway aligns well with the intermediates identified electrochemically and the characteristic spectral features observed during NO_3^-RR.[46]

Based on the XRD and SEM characterization results, a corresponding structural model was constructed (Fig. S23). The density of states (DOS) analysis (Fig. 4d) demonstrated that Si doping shifted the occupied electron states closer to the Fermi energy level, resulting in a higher DOS for Si-ZnCo-LDH/Cu. The d-band centers of ZnCo-LDH/Cu and Si-ZnCo-LDH/Cu were −3.44 and −2.48 eV, respectively. Based on the d-band center theory, a higher d-band center indicates stronger interactions with intermediates, high lighting the improved catalytic potential of Si-ZnCo-LDH/Cu. The differential charge density and Bader charge analyses (Fig. 4e and S24) further investigated the charge transfer processes between active site and NO_3^- species in ZnCo-LDH/Cu and Si-ZnCo-LDH/Cu. The results show that in the Si-ZnCo-LDH/Cu catalyst, due to the obvious charge distribution around the silicon-doped Co atoms, the charge transferred to the adsorbed NO_3^- is greater compared with ZnCo-LDH/Cu. Among them, the Co atom in ZnCo-LDH/Cu transferred 0.75 electrons to the nearby O atom, while the Co atom in Si-ZnCo-LDH/Cu transferred 1.05 electrons to the surrounding O atom. This suggests that Si doping modulates the local electron density around Co active sites and optimizes the intermediate adsorption *via* the formed M–O–Si linkages. This configuration facilitates interfacial electron aggregation and promotes efficient charge transfer to adsorbed intermediates (*e.g.*, NO_3^-), thereby boosting the catalytic performance.

Density functional theory (DFT) calculations indicated that the fundamental pathway for the reduction of NO_3^- to NH_3 on the catalyst surface proceeds as follows: NO_3^- is first adsorbed to form $*NO_3$, accompanied by a decrease in the total energy. This is followed by the spontaneous and

sequential cleavage of the N–O bond in $*NO_3$, generating $*NO_2$ and *NO. The *NO intermediate then undergoes hydrogenation to form *NOH, which is further hydrogenated to $*NH_2OH$ and finally converted to $*NH_3$ before desorbing from the catalyst surface.[47,48] We also computed the Gibbs free energies for each intermediate involved in the electrocatalytic NO_3^-RR, as well as those related to the competing hydrogen evolution reaction (HER), for both ZnCo-LDH/Cu and Si-ZnCo-LDH/Cu catalysts (Fig. 4f). As shown in Fig. 4g, the hydrogenation of *NO to *NOH (*NO + *H → *NOH) constitutes the rate-determining step (RDS) for ammonia synthesis *via* NO_3^-RR on both catalysts. Notably, Si-ZnCo-LDH/Cu markedly promotes the formation of the *NOH intermediate compared to ZnCo-LDH/Cu, thereby facilitating the electrocatalytic hydrogenation process. DFT calculation further elucidate the bifunctional modulation mechanism induced by Si doping in ZnCo-LDH/Cu (Fig. S25 and S26). The free energy barrier for the RDS (*NO → *NOH) in NO_3^-RR is significantly reduced from 0.97 eV for the undoped catalyst to 0.51 eV for the Si-doped sample-a decrease of 47.4%. This effect originates from specific interactions between the Si–O site and the *NO intermediate: (1) the strong Lewis acidity of Si promotes polarization of the N–O bond, and (2) charge transfer from Si–O to the N atom reduces the electron density at N, accelerating the proton-coupled electron transfer process. Concurrently, Si doping increases the adsorption free energy of H^+ by 0.35 eV, which effectively suppresses the competing HER.[49] This selective activation mechanism results in a remarkable enhancement in both the ammonia synthesis rate and the faradaic efficiency (increasing from 58.41% to 93.61%) for Si-ZnCo-LDH/Cu over the undoped catalyst, achieving a synergistic optimization of activity and selectivity.

Application in Zn–NO_3^- battery

Building on the excellent nitrate reduction performance of Si-ZnCo-LDH/Cu, we assembled a Zn–NO_3^- battery system in an H-type electrolyzer (Fig. 5a), achieving the integrated goals of ammonia synthesis, power generation, and wastewater treatment. The cathode (Si-ZnCo-LDH/Cu) and anode (zinc foil) were immersed in 0.5 M Na_2SO_4 (with 0.1 M NO_3^-) and 6 M KOH (with 0.2 M $Zn(CH_3COO)_2$) electrolytes, respectively. The battery exhibited an open-circuit potential of 1.432 V (*vs.* Zn/Zn^{2+}, Fig. 5b), indicating a substantial thermodynamic driving force. As shown in Fig. 5c, the Zn–NO_3^- battery based on Si-ZnCo-LDH/Cu delivered a peak power density of 17 mW cm^{-2} at a current density of 56 mA cm^{-2}, confirming its efficient energy output capability.[50]

The battery demonstrated excellent rate performance and a stable voltage response during galvanostatic testing over a wide current density range of 2–10 mA cm^{-2} (Fig. 5d), highlighting the structural stability and favourable reaction kinetics of the electrode under varying current conditions.[51,52] In terms of NO_3^-RR performance (Fig. 5e), the ammonia production rate increased significantly with current density from 10 to 30 mA cm^{-2}, reaching a peak value of 1294.44 μg h^{-1} cm^{-2} at 30 mA cm^{-2}, underscoring the

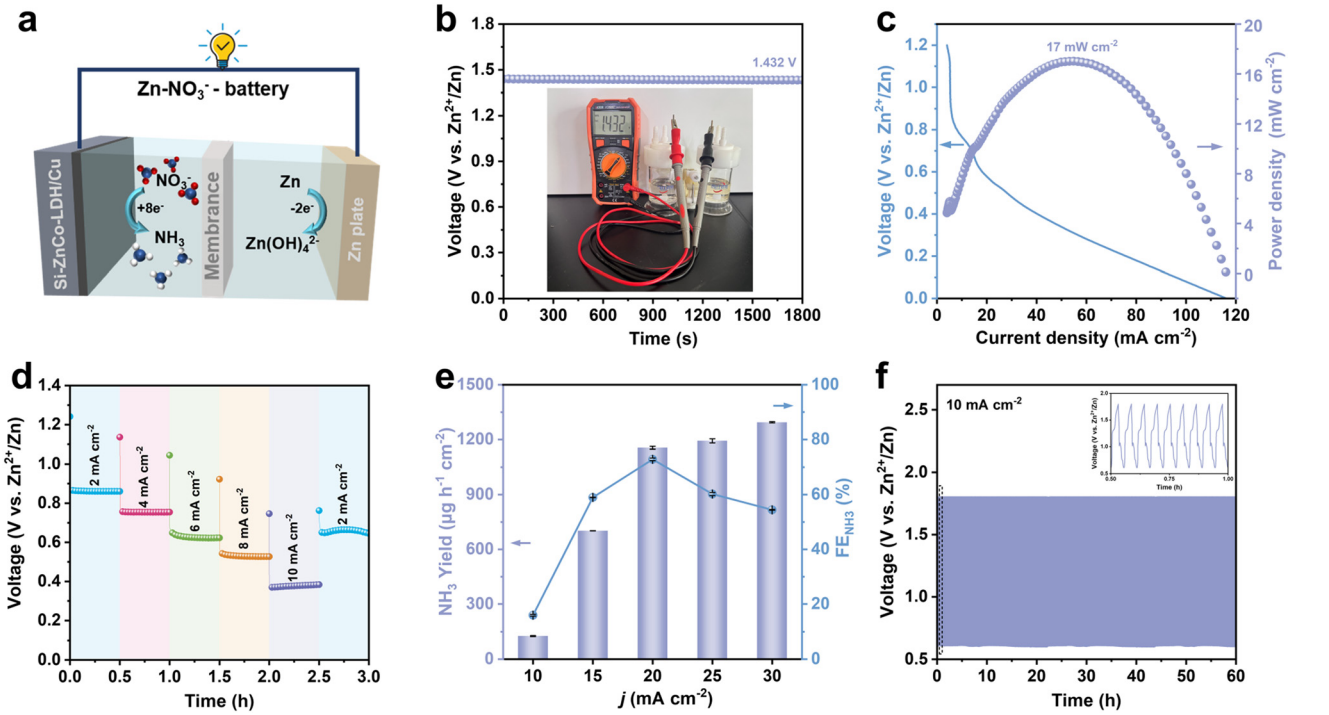

Fig. 5 Zn–NO_3^- battery performance. (a) Schematic diagram of the battery. (b) Open-circuit potential in the stationary state. (c) Discharge polarization curve and power density curve. (d) Discharge test results at different current densities. (e) Ammonia yield and FE during the discharge process. (f) The charge and discharge cycle curves under the condition of 10 mA cm^{-2} and the corresponding first 9 cycles (inset).

outstanding catalytic activity of the catalyst for nitrate reduction at high current densities. Meanwhile, the Faradaic efficiency reached a maximum of 72.87% at 20 mA cm^{-2}, indicating high selectivity for electron transfer and effective suppression of competing side reactions such as the HER under this condition.[53]

During operation, the anode undergoes Zn dissolution and deposition, while the cathode reduces nitrate to ammonia during discharge and evolves oxygen during charging.[49] Charge–discharge cycling tests performed at a constant current density of 10 mA cm^{-2} (Fig. 5f) showed stable operation over 60 hours with minimal voltage fluctuation, fully verifying the stability and reliability of the battery system and catalyst structure during long-term operation. These results demonstrate that the assembled Si-ZnCo-LDH/Cu-based Zn–NO_3^- battery exhibits high power output, excellent nitrate reduction activity, and good cycling stability, providing an important reference for the development of efficient Zn–NO_3^- battery systems.

Conclusions

In summary, a silicon-doped ZnCo layered double hydroxide (Si-ZnCo-LDH) electrocatalyst was successfully synthesized through a facile 30 second room-temperature etching approach. The optimized electrode achieved an exceptional Faradaic efficiency of 93.6% for NH_3 production and a high generation rate of 25.71 mg h^{-1} cm^{-2} in neutral electrolyte, significantly outperforming the undoped counterpart. Systematic investigations confirm that the introduced "M–O–Si" motifs play a pivotal role by optimizing the electronic structure and substantially lowering the energy barrier of the rate-determining step (*NO → *NOH), thereby favoring the selective pathway toward ammonia formation and suppressing competing hydrogen evolution. When integrated into a Zn–NO_3^- battery, the catalyst delivered a maximum power density of 17 mW cm^{-2} and maintained stable performance over 60 hours, demonstrating its practical potential. This work establishes silicon doping as a powerful and versatile strategy for electronic structure engineering in layered double hydroxides, offering a general design principle for advanced electrocatalysts.

Author contributions

Kunxuan Zhao: writing – review & editing, writing – original draft, visualization, validation, resources, methodology, investigation, formal analysis, data curation, conceptualization. Pei Chen: visualization, validation, resources, methodology, software, investigation, formal analysis, data curation. Yulan Shi: resources, methodology, investigation, formal analysis, data curation. Zhen Yang: writing – resources, investigation, data curation, conceptualization. Xia Zhou: supervision, investigation, formal analysis, validation, data curation. Jinfeng Yang: writing – review & editing, writing – original draft, visualization, validation, resources, methodology, software, supervision, investigation, formal analysis, data curation, conceptualization. Xiaodong Yang: validation, software, investigation, DFT simulations. Feng Yu: writing – review editing, writing – original draft, visualization, validation, resources, methodology, software, supervision, investigation, formal analysis, data curation, conceptualization.

Conflicts of interest

There are no conflicts to declare.

Data availability

Data will be made available on request.

Supplementary information (SI): Experimental, Fig. S1–S26 and Tables S1–S5. See DOI: https://doi.org/10.1039/d6cy00140h.

Acknowledgements

We acknowledge the financial support from the Xinjiang Science and Technology Program (2023TSYCCX0118) and High-Level Talent Research Initiation Program at Shihezi University (RCZK202528).

References

1 Y. Zuo, M. Sun, T. Li, L. Sun, S. Han, Y. Chai, B. Huang and X. Wang, *Adv. Mater.*, 2025, **37**, 2415632.
2 T. Xiang, X. Liu, Z. Wang, Y. Zeng, J. Deng, W. Xiong, M. Cheng, J. Liu, C. Zhou and Y. Yang, *Appl. Catal., B*, 2025, **365**, 124943.
3 Q. Wu, D. Shao, C. Dai, J. Wang, X. Li, P. Song, W. Xie, S. Xi, L. Zhang, X. Lin, S. Luo, S. Sun, L. An, P. Xi and Z. J. Xu, *J. Am. Chem. Soc.*, 2025, **147**, 30401–30411.
4 X. Shi, W.-H. Huang, J. Rong, M. Xie, Q. Wa, P. Zhang, H. Wei, H. Zhou, M.-H. Yeh, C.-W. Pao, J. Wang, Z. Hu, X. Yu, J. Ma and H. Cheng, *Nat. Commun.*, 2025, **16**, 6161.
5 F. Shen, S. He, X. Tang, Y. Liu, Y. Wang, Y. Yin, X. Lv, W. Fu, Y. Zou, G. Jiang and L. a. Hou, *Angew. Chem., Int. Ed.*, 2025, **64**, e202423154.
6 F. Yu, *Huagong Jinzhan*, 2023, **42**, 6136–6140.
7 F. Yu, *Int. J. Hydrogen Energy*, 2024, **61**, 1043–1046.
8 L. Lv, H. Tan, Y. Liu, N. Li, Q. Ji, Y. Kong, H. Wang, M. Sun, M. Fan, C. Wang and W. Yan, *Adv. Funct. Mater.*, 2025, **35**, 2423612.
9 Y. Lu, F. Yue, T. Liu, Y.-C. Huang, F. Fu, Y. Jing, H. Yang and C. Yang, *Nat. Commun.*, 2025, **16**, 2392.
10 Q. Hu, C. Shang, X. Chen, S. Qi, Q. Huo, H. Yang and C. He, *J. Am. Chem. Soc.*, 2025, **147**, 12228–12238.
11 X. Long, B. Zhao, D. Liu, G. Fu, H. Yang, R. Feng, N. Chen, H. Ding, J. Wu, Y. Liao, S. Liu, Y. Zhang, X. Z. Fu and J. L. Luo, *Angew. Chem., Int. Ed.*, 2025, **64**, e202503424.
12 P. H. van Langevelde, I. Katsounaros and M. T. M. Koper, *Joule*, 2021, **5**, 290–294.
13 F.-Y. Chen, Z.-Y. Wu, S. Gupta, D. J. Rivera, S. V. Lambeets, S. Pecaut, J. Y. T. Kim, P. Zhu, Y. Z. Finfrock, D. M. Meira, G. King,

G. Gao, W. Xu, D. A. Cullen, H. Zhou, Y. Han, D. E. Perea, C. L. Muhich and H. Wang, *Nat. Nanotechnol.*, 2022, **17**, 759–767.
14 S. Z. Andersen, V. Čolić, S. Yang, J. A. Schwalbe, A. C. Nielander, J. M. McEnaney, K. Enemark-Rasmussen, J. G. Baker, A. R. Singh, B. A. Rohr, M. J. Statt, S. J. Blair, S. Mezzavilla, J. Kibsgaard, P. C. K. Vesborg, M. Cargnello, S. F. Bent, T. F. Jaramillo, I. E. L. Stephens, J. K. Nørskov and I. Chorkendorff, *Nature*, 2019, **570**, 504–508.
15 H.-R. Li, X. Kang, R. Gao, M.-M. Shi, B. Bi, Z.-Y. Chen and J.-M. Yan, *Chin. Chem. Lett.*, 2025, **36**, 109958.
16 S. Zheng, F. Zhang, Y. Jiang, T. Xu, H. Li, H. Guo and Y. Zhou, *Front. Chem. Sci. Eng.*, 2024, **18**, 112.
17 Z.-Q. Ge, C. Chu, C. Wang, R. Li, J. Li and S. P. Jiang, *Science for Energy and Environment*, 2024, **1**, 10.
18 W. Wang, J. Chen and E. C. M. Tse, *J. Am. Chem. Soc.*, 2023, **145**, 26678–26687.
19 X. Zhang, X. Liu, Z.-F. Huang, L. Guo, L. Gan, S. Zhang, M. Ajmal, L. Pan, C. Shi, X. Zhang, G. Yang and J.-J. Zou, *ACS Catal.*, 2023, **13**, 14670–14679.
20 X. Gu, J. Zhang, S. Guo, Y. Zhang, L. Xu, R. Jin and G. Li, *J. Am. Chem. Soc.*, 2025, **147**, 22785–22795.
21 Y. Fu, Y. Li, F. Fan, B. Chen, X. Hou, Y. Li, H. Li, Y. Fu and W. Qi, *ACS Catal.*, 2025, **15**, 6918–6928.
22 Y. Q. Xu, Z. L. Wang, L. Tan, Y. F. Zhao, H. H. Duan and Y. F. Song, *Ind. Eng. Chem. Res.*, 2018, **57**, 10411–10420.
23 F. Lin, H. Luo, L. Li, F. Lv, Y. Chen, Q. Zhang, X. Han, D. Wang, M. Li, Y. Luo, K. Wang, L. Gu, Q. Wang, X. Zhao, M. Luo and S. Guo, *Nat. Synth.*, 2024, **4**, 399–409.
24 Y. Wei, Z. Xiao, Y. Huang, Y. Zhu, Z. Zhu, Q. Zhang, D. Jia, S. Zhang and F. Wei, *Small*, 2023, **20**, 2310240.
25 H. Gao, P. Fu, J. Yu, X. Yang, Y. Tang, Y. Zhao, S. Yang, G. Wang, F. Yu and Y. Li, *Electrochim. Acta*, 2024, **498**, 144649.
26 W. Fu, Z. Hu, Y. Zheng, P. Su, Q. Zhang, Y. Jiao and M. Zhou, *Chem. Eng. J.*, 2022, **433**, 133680.
27 S. Hoekx, N. Daems, D. Arenas Esteban, S. Bals and T. Breugelmans, *ACS Appl. Energy Mater.*, 2024, **7**, 3761–3775.
28 H. Yin, Z. Chen, S. Xiong, J. Chen, C. Wang, R. Wang, Y. Kuwahara, J. Luo, H. Yamashita, Y. Peng and J. Li, *Chem Catal.*, 2021, **1**, 1088–1103.
29 Y.-S. Tsai, S.-C. Yang, T.-H. Yang, C.-H. Wu, T.-C. Lin and C.-W. Kung, *ACS Appl. Mater. Interfaces*, 2024, **16**, 62185–62194.
30 Y. Xu, Y. Sheng, M. Wang, T. Ren, K. Shi, Z. Wang, X. Li, L. Wang and H. Wang, *J. Mater. Chem. A*, 2022, **10**, 16883–16890.
31 X. Cheng, Z. Xie, S. Zha, Q. Xu, S. Ci and Z. Wen, *J. Mater. Chem. A*, 2025, **13**, 13286–13294.
32 J. Yang, H. Qi, A. Li, X. Liu, X. Yang, S. Zhang, Q. Zhao, Q. Jiang, Y. Su, L. Zhang, J.-F. Li, Z.-Q. Tian, W. Liu, A. Wang and T. Zhang, *J. Am. Chem. Soc.*, 2022, **144**, 12062–12071.
33 F. Zhao, G. Hai, X. Li, Z. Jiang and H. Wang, *Chem. Eng. J.*, 2023, **461**, 141960.
34 J. Qin, L. Chen, K. Wu, X. Wang, Q. Zhao, L. Li, B. Liu and Z. Ye, *ACS Appl. Energy Mater.*, 2021, **5**, 71–76.
35 C. Li, S. Liu, Y. Xu, T. Ren, Y. Guo, Z. Wang, X. Li, L. Wang and H. Wang, *Nanoscale*, 2022, **14**, 12332–12338.
36 T. Ren, K. Ren, M. Wang, M. Liu, Z. Wang, H. Wang, X. Li, L. Wang and Y. Xu, *Chem. Eng. J.*, 2021, **426**, 130759.
37 Z. Zhang, B. Ge, M. Liu, T. Yang, S. Wang, Y. Liu, Y. Yang and S. Gao, *ACS Appl. Mater. Interfaces*, 2025, **17**, 26501–26510.
38 S.-N. Zhang, P. Gao, Q.-Y. Liu, Z. Zhang, B.-L. Leng, J.-S. Chen and X.-H. Li, *Nat. Commun.*, 2024, **15**, 10877.
39 Y. Wan, M. Pei, Y. Tang, Y. Liu, W. Yan, J. Zhang and R. Lv, *Adv. Mater.*, 2025, **37**, 2417696.
40 Y. You, H. Chen, J. Guo, Z. Feng, J. Zhan, F. Yu and L.-H. Zhang, *Appl. Catal., B*, 2025, **363**, 124837.
41 S. Liang, X. Teng, H. Xu, L. Chen and J. Shi, *Angew. Chem.*, 2024, **136**, e202400206.
42 S. Lu, G. Lin, H. Yan, Y. Li, T. Qi, Y. Li, S. Liang and L. Jiang, *ACS Catal.*, 2024, **14**, 14887–14894.
43 X. Zhang, W. H. Li, J. Zhang, H. S. Zhou and M. Zhong, *Chin. J. Catal.*, 2025, **68**, 404–413.
44 C. M. Yang, T. T. Wei, C. T. Wang, F. Yue, X. Li, H. J. Pang, X. Y. Zheng, Y. T. Zhang and F. Fu, *Mater. Horiz.*, 2025, **12**, 877–885.
45 S. Zhang, J. Wu, M. Zheng, X. Jin, Z. Shen, Z. Li, Y. Wang, Q. Wang, X. Wang, H. Wei, J. Zhang, P. Wang, S. Zhang, L. Yu, L. Dong, Q. Zhu, H. Zhang and J. Lu, *Nat. Commun.*, 2023, **14**, 3634.
46 H. Luo, S. Li, Z. Wu, Y. Liu, W. Luo, W. Li, D. Zhang, J. Chen and J. Yang, *Adv. Mater.*, 2023, **35**, 2304695.
47 Z. Wu, Y. Song, H. Guo, F. Xie, Y. Cong, M. Kuang and J. Yang, *Interdiscip. Mater.*, 2024, **3**, 245–269.
48 J. Guan, L. Cai, W. Li, H. Zhou and Y. Huang, *Appl. Catal., B*, 2024, **358**, 124387.
49 Z. Chen, Y. Zhao, H. Huang, G. Liu, H. Zhang, Y. Yan, H. Li, L. Liu, M. Liu, D. Wang and J. Zeng, *J. Am. Chem. Soc.*, 2025, **147**, 18737–18746.
50 W. Zhang, X. Zhang, Y. Zhou, S. Li, T. Wang, Z. Wu and R. Li, *Cell Rep. Phys. Sci.*, 2025, **6**, 102606.
51 H. Jiang, G. F. Chen, O. Savateev, J. Xue, L. X. Ding, Z. Liang, M. Antonietti and H. Wang, *Angew. Chem.*, 2023, **135**, e202218717.
52 M. Chen, X. Li, N. Liu, Z. Du, Z. Wang and J. Qi, *Chin. Chem. Lett.*, 2025, **36**, 111294.
53 W. Chen, Z. Sun, S. Zhen, Y. Wang, J. Sun, M. Liu, W. J. Han, L. Lai, W. Wei, L. Zhang and W. Chen, *Adv. Funct. Mater.*, 2025, e09200.